ADVANCING EARTH AND SPACE SCIENCES

Geophysical Research Letters

RESEARCH LETTER
10.1029/2023GL103704

Key Points:

- Interferometric synthetic aperture radar data are used to study ground deformation before, during and after the 2022 Wolf eruption
- A ring fault opening/closure model fits ground deformation of the caldera well
- Asymmetric opening of the ring fault promotes flank eruptions at Wolf volcano

Supporting Information:

Supporting Information may be found in the online version of this article.

Correspondence to:

W. Xu,
wenbin.xu@csu.edu.cn

Citation:

Xu, W., Xie, L., Bürgmann, R., Liu, X., & Wang, J. (2023). The 2022 eruption of Wolf volcano, Galápagos: The role of caldera ring-faults during magma transfer from InSAR deformation data. *Geophysical Research Letters*, *50*, e2023GL103704. https://doi.org/10.1029/2023GL103704

Received 21 MAR 2023
Accepted 7 JUL 2023

Author Contributions:

Conceptualization: Wenbin Xu
Data curation: Lei Xie
Formal analysis: Wenbin Xu, Lei Xie
Funding acquisition: Wenbin Xu
Investigation: Wenbin Xu, Lei Xie, Roland Bürgmann
Methodology: Wenbin Xu
Resources: Wenbin Xu
Supervision: Wenbin Xu
Visualization: Wenbin Xu, Lei Xie
Writing – original draft: Wenbin Xu
Writing – review & editing: Wenbin Xu, Roland Bürgmann

The 2022 Eruption of Wolf Volcano, Galápagos: The Role of Caldera Ring-Faults During Magma Transfer From InSAR Deformation Data

Wenbin Xu[1,2], Lei Xie[1,2], Roland Bürgmann[3], Xiaoge Liu[1,2], and Jiageng Wang[1,2]

[1]Lab of Volcano and Earthquake Research, School of Geosciences and Info-Physics, Central South University, Changsha, China, [2]Key Laboratory of Metallogenic Prediction of Nonferrous Metals and Geological Environment Monitoring, Central South University, Changsha, China, [3]Department of Earth and Planetary Science, University of California, Berkeley, CA, USA

Abstract The basaltic caldera volcanoes in the Galápagos Islands characteristically erupt lavas via summit circumferential and radial flank dike intrusions, but the underlying magma plumbing systems remain enigmatic. Here, we document surface displacements of Wolf volcano using interferometric synthetic aperture radar (InSAR) data from 2015 to 2022. We show that Wolf volcano experienced 6-years of continuous inflation after the 2015 eruption, followed by a shallow flank eruption in January 2022. The deformation is modeled with a vertical caldera ring-fault and a radial dike on the southeast flank. The ring-fault underwent opening and reverse faulting during the inflation period, and closure and normal faulting during and after the eruption. Stress interactions between the ring-fault and the flank dike suggest the asymmetric opening of the ring-fault promotes flank eruptions. The best-fit deformation model differs from the previous models and offers an alternative view of how magma is fed into radial dikes during flank eruptions.

Plain Language Summary The 2022 eruption at Wolf volcano in the Galápagos Islands started from a radial fissure on the SE flank, which was different from the 2015 eruption that mainly occurred inside the caldera. We track the sequence of ground deformation before, during and after the 2022 eruption using InSAR data. We find that Wolf volcano experienced continuous inflation before the 2022 eruption, followed by deflation during and after the eruption, resulting in complex ground deformation within and beyond the caldera and on the SE flank. We propose a model with ring fault slip and opening/closure to explain the observed ground deformation within the caldera. We find that opening and reverse slip of the ring fault can explain the inflation before the 2022 eruption, while closure and normal slip caused the deflation period during and after the eruption. The asymmetric opening of the ring fault changed the stresses in the volcano and promoted the occurrence of the flank eruption. Our model is different from the dike rotation model that was proposed for Fernandina volcano and may allow for improved forecasts of the location and style of future eruptions on the Galapagos Islands.

1. Introduction

The Galápagos Islands sit atop a mantle hotspot centered beneath Fernandina and Isabela islands and constitute one of the world's largest and most active groups of oceanic volcanoes (Geist et al., 2014; Ito & Bianco, 2014). Six out of seven volcanoes of the western Galápagos Islands have well-developed summit calderas (Figure 1). Frequent eruptions have been reported in the Galápagos since the 1950s (Simkin & Siebert, 1994) and caldera collapse was witnessed at Fernandina Volcano in 1968 (Howard et al., 2018). Interferometric synthetic aperture radar (InSAR) data show both eruptive and precursory ground deformation on these caldera volcanoes, four of which have erupted since 2000 (Amelung et al., 2000; Bernard et al., 2019).

Wolf volcano is the highest and one of the most active volcanoes in the Galápagos Islands. Young lava flows have covered a large portion of the volcano's subaerial surface especially on the southeastern half of the volcano (Chadwick and Howard., 1991; Geist et al., 2005). It has a well-developed arcuate summit and radial flank eruptive fissure system. Wolf volcano has experienced eight eruptions during the past 100 years (Bernard et al., 2019). Recent eruptions at Wolf volcano occurred in 1982 and 2015, producing lava fountains and flows within the summit caldera and on the flanks. The estimated net areal coverage of subaerial lava during these two eruptions is about 33 km^2 (Bernard et al., 2019).

10.1029/2023GL103704

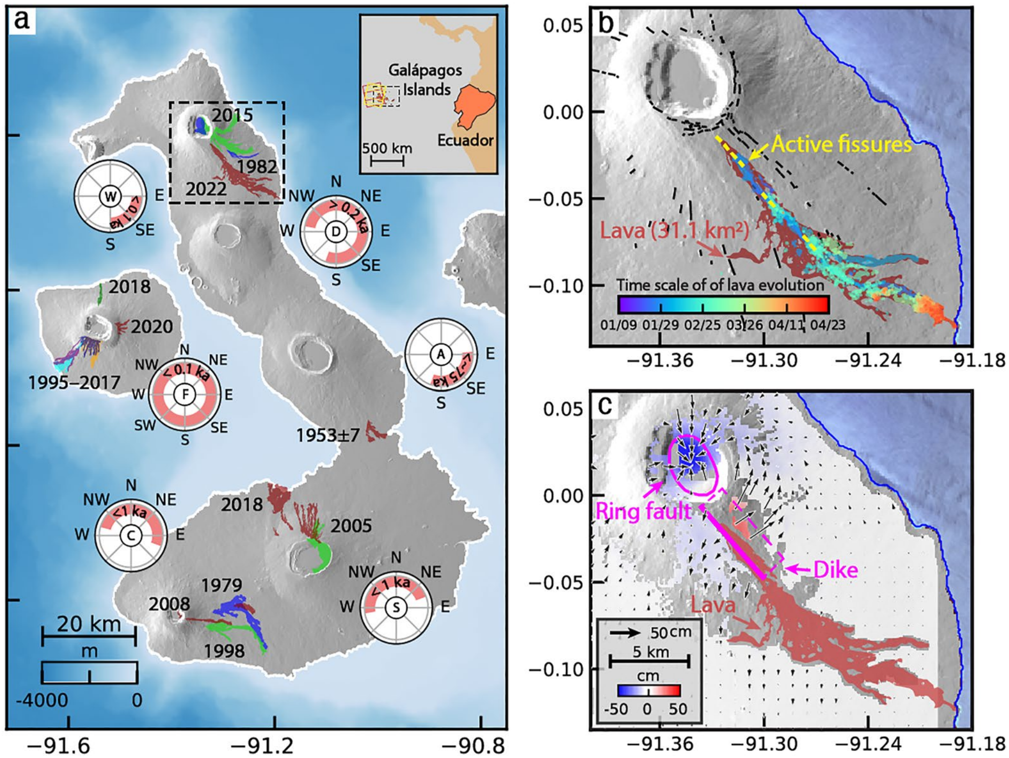

Figure 1. Locations of recent eruptions in the western Galápagos Islands. (a) Polar charts and mapped flows show the dates and directions of recent lava flows from historical eruption records, letter at center of each polar chart is the first letter of each volcano name (Bagnardi et al., 2013; Bernard et al., 2019, 2022; Chadwick et al., 2011; Galetto et al., 2020; Geist et al., 2008; Rowland et al., 2003; Teasdale et al., 2005; Vasconez et al., 2018). The 3 arc-second bathymetry map is from the National Oceanic and Atmospheric Administration (https://www.ncei.noaa.gov/maps/bathymetry/). The dashed box shows the areas of (b) and (c). Inset shows the location of Galápagos Islands in relation to Ecuador and South America. Ascending and descending SAR image frames are shown in red and yellow rectangles. (b) Color-coded areas represent the evolution of lava flows from January to April associated with the 2022 eruption. Eruptive fissures are marked as yellow dashed lines. The dark-red polygon indicates the total coverage of lava flows with an estimated area of 31 km^2. Mapped historical eruptive fissures are shown as black lines. (c) 3D surface displacements of the 2022 eruption from InSAR LOS and azimuth displacement data. The background color map shows vertical and arrows indicate horizontal displacements. The gaps in data coverage with background topography (gray) denote areas without reliable InSAR deformation retrievals due to the loss of coherence. The surface projections of the modeled ring fault and flank dike are shown in magenta.

Given that Wolf volcano is in a remote and uninhabited area, where no in situ geodetic and geophysical instruments have been installed to monitor volcanic and earthquake activity, satellite remote sensing data provide essential information to understand the course of deformation associated with eruptions, and to track the lava flows they produce. A dense time-series of satellite optical imagery shows the emplacement of lava flows from 9 January to 16 April 2022 (Figure S1 in Supporting Information S1). At least four active fissures opened from higher to lower altitudes trending about 141° on the southeastern flank (Figure 1). One lava flow reached about 15 km from the highest eruptive fissure on 11 January 2022. The activity progressed to the lower flank fissure, sending out fresh lava on 16 January 2022. By 16 April 2022, the lava had traveled about 18.5 km from the uppermost vent, covering a total subaerial area of about 31 km^2. No active lava flows were observed after 20 April 2022.

2. Data and Methods

2.1. Subaerial Lava Evolution From Optical Imagery

We collected high-resolution satellite optical images to track the evolution of lava flows during the 2022 eruption (Sentinel-2, Landsat-8/9, PlanetScope) (Figure S1 and Table S1 in Supporting Information S1). For the optical data with multiple thermal bands (e.g., Sentinel-2 and Landsat-8/9), we applied a clustering algorithm to consider

10.1029/2023GL103704

both the spectral and spatial properties (Massimetti et al., 2020). First, the active hot-spot pixels were grouped by four reflectance indices using the short-wave infrared (SWIR) and near-infrared (NIR) bands (Bands 12-11-8A for Sentinel-2, and Bands 7-6-5 for Landsat), as follows:

$$C = \begin{cases} \left(\frac{SWIR2}{SWIR1} \geq 1.4\right) \cap \left(\frac{SWIR2}{NIR} \geq 1.2\right) \cap (SWIR2 \geq 0.15) \\ \left(\frac{SWIR1}{NIR} \geq 2\right) \cap (SWIR1 \geq 0.5) \cap (SWIR2 \geq 0.5) \\ [(SWIR2 \geq 1.2) \cap (NIR \leq 1)] \cup [(SWIR1 \geq 1.5) \cap (NIR \geq 1)] \\ (SWIR2 \geq 1) \cap (SWIR1 \geq 1) \cap (NIR \geq 0.5) \end{cases} \tag{1}$$

The first two indices represent the hot-spot-contaminated pixels, and the third and fourth conditions correspond to the remaining thermally saturated pixels and reflective pixels, respectively. Therefore, the pixels that satisfy either of these conditions are labeled as the hot-spot candidates. We then formulated an empirical thermal index from a thermal band combination $TI = SWIR1 + SWIR2 + NIR$ as the proxy of lava temperature allowing us to perform a frequency distribution analysis. The pixels in the lower tail of the thermal distribution were removed owing to possible contamination (e.g., halo and blurring) from surrounding lava flows. For the single-band thermal image (i.e., PlanetScope), we directly set the cut-off threshold on the NIR band by maximum interclass variance to map the fresh lava. Because of the dense cloud coverage and substantial ash emissions, we manually delineated the total coverage of lava fields from post-eruption optical images and SAR amplitude data.

2.2. InSAR Data Processing

We used the ISCE software (Rosen et al., 2012) to undertake the interferogram processing of SAR data from the Japanese Aerospace Exploration Agency's ALOS-2 and the European Space Agency's Sentinel-1 satellites. We applied the network-based enhanced spectral diversity (Fattahi et al., 2017) method for coregistration to ensure a 1/1000-pixel accuracy. The topographic phase components were estimated from the one arc-sec Shuttle Radar Topography Mission Digital Elevation Model (SRTM DEM), and we filtered and unwrapped the interferograms using the power spectrum filter and the minimum cost flow method, respectively. InSAR measures ground deformation along the radar line of sight (LOS) direction. We also used the multiple aperture InSAR method to calculate horizontal displacements in the flight direction using ALOS-2 data (Bechor & Zebker, 2006). The azimuth deformation was then combined with the LOS displacements to resolve the 3D displacements associated with the 2022 eruption (Fialko et al., 2001). The posteruptive deformation maps were constructed using descending Sentinel-1 SAR images between 29 January and 14 September 2022. Only a few scenes were available in the ascending orbit during the posteruptive period, because of a power bus failure on the Sentinel-1B satellite. The resultant interferograms were resampled to 60 m spatial resolution and geocoded to the World Geodetic System 1984 geodetic datum.

To resolve the temporal evolution of surface displacement and mean velocity, we used a linear optimization small baseline subsets method with a weighted least squares estimator provided by the Mintpy software package (Zhang et al., 2019). We processed 242 ascending and 315 descending Sentinel-1 SAR SLC images between 17 July 2015 and 14 September 2022. Each acquisition was paired with its five nearest images, generating 1111 ascending and 1555 descending interferograms (Table S2 in Supporting Information S1). We masked out the incoherent areas within the caldera that coincided with the erupted lavas from the 2015 event, where lava cooling and compaction perturb the signal (Poland & Carbone, 2016; Xu & Jónsson, 2014). We corrected the phase unwrapping errors based on the interferogram phase closure triplets. After solving the raw phase time-series, we separated the tropospheric delay using the ERA5 reanalysis products (Hersbach et al., 2020) from the European Center for Medium-range Weather Forecasts and corrected the topography-correlated atmospheric noise from the phase velocity history in the time domain (Fattahi & Amelung, 2013).

2.3. Data Inversion Method

We started by modeling the co-eruptive InSAR data because these data show two apparent deformation sources. These are a shallow dike feeding the eruptive fissures on the southeast flank and another source responsible for the volcano-wide deformation. We modeled these sources using rectangular dislocations (Okada, 1985) by assuming a homogeneous and isotropic elastic half-space, ignoring the effects of topography in the modeling (Williams & Wadge, 2000). Many existing studies have shown that including the topography in the modeling broadens the predicted deformation, but the effects are secondary (Xu et al., 2016).

We subsampled the data points using the quadtree method (Jónsson, 2002) and weighed the data according to their variance. We first developed a model of the shallow source on the southeast flank as it produces a distinct deformation pattern associated with a dike intrusion. We used the mapped fissures from high-resolution optical imagery (Figure S1 in Supporting Information S1) to set the location and strike of the dike. We then searched for its optimal dip and uniform opening that minimizes the weighted root-mean-square misfit between the cumulative deformation and the model predictions. We estimated the best-fitting model parameters by using a Monte Carlo-type simulated annealing algorithm (Cervelli et al., 2001), followed by a gradient-based method. Finally, we applied least squares inversion to determine the distributed finite dike opening that best fits the InSAR datasets.

Once the source parameters of the dike were found, we estimated the parameters of the deformation source within the caldera. Previous studies have suggested that a two-sill model, or a combined deep sill and ring fault model can match the observed ground deformation within and outside the caldera (Liu et al., 2019; Stock et al., 2018; Xu et al., 2016). The two-sill model assumes that the deep and shallow sources are hydraulically connected, while the combined deep sill and ring fault model assumes that when the deep sill expands, it might trigger slip on the lowermost part of the ring fault, leading to a concentration of deformation within the caldera. However, this model has not yet been tested using InSAR data.

Because dikes often intrude along the ring fault within caldera volcanoes in nature (Gudmundsson et al., 2016) and circumferential and radial dikes may alternate in time on a given volcano flank (Chadwick & Dieterich, 1995), we propose a new model scenario that involves ring fault slip together with opening and closing of the ring fault zone due to magma intrusion and withdrawal in the years leading up to and during the 2022 eruption at Wolf volcano. That is, the ring fault zone acts both as a roughly circular dike structure (effectively a circumferential dike) and also accommodates vertical shear during the caldera inflation/deflation cycle. This proposed model allows us to examine the relationship between the volcano-wide deformation and the deep source. We explore how the observed ground deformation before, during and after the 2022 eruption can constrain the source parameters. We compare the RMS data misfit of this model with that of the two previously proposed source configurations (Liu et al., 2019; Xu et al., 2016) to find the optimal model and evaluate the influence of replacing the deep sill by a ring fault with both slip and opening/closure.

We approximate the ring fault by a cylindrical fault plane with a vertical dip, allowing discrete fault patches to slip in the dip-direction, as well as to open and close during times of magma intrusion and loss. In this context, we define reverse slip along the ring fault as due to the inside of the cylinder moving upwards and normal slip as the inside moving downward. The steep ring fault geometry is consistent with predictions from experimental studies and observations elsewhere (Bell et al., 2021; Liu et al., 2019). The location of the caldera ring fault is fixed to the outline of the caldera, and the bottom reaches to 6 km beneath the caldera floor where it meets a deep sill-like reservoir found in previous studies (Geist et al., 2005). Once the geometry of the ring fault is set up, we apply least squares inversion to determine the distribution of finite opening/closure and slip along the ring fault for the co-eruptive InSAR datasets. Because no ascending Sentinel-1 data are available before January 2017 and after March 2022, we use the ascending and descending pre-eruptive data between January 2017 and January 2022 and the descending post-eruptive data to estimate the finite source values of the ring fault in a linear least squares inversion, respectively.

2.4. Stress Change Calculations

We use Coulomb 3 software (Lin & Stein, 2004) to calculate the static normal-stress change transferred to the 2022 dike plane and the ring fault from the 2017–2022 ring-fault opening and reverse-slip model inverted from the InSAR time-series deformation. Positive normal-stress changes indicate dike unclamping. During the normal-stress calculation, the source fault is the modeled vertical ring fault, and the targeted receiver faults are the ring fault itself and the radial dike that fed the 2022 eruption.

3. Results

3.1. Pre-Eruptive Deformation During 2015–2022

We used InSAR data acquired by the Sentinel-1 satellite between 17 July 2015 and 5 January 2022 to map the ground deformation before the 2022 flank fissure eruption. A stack of the pre-eruptive interferograms shows

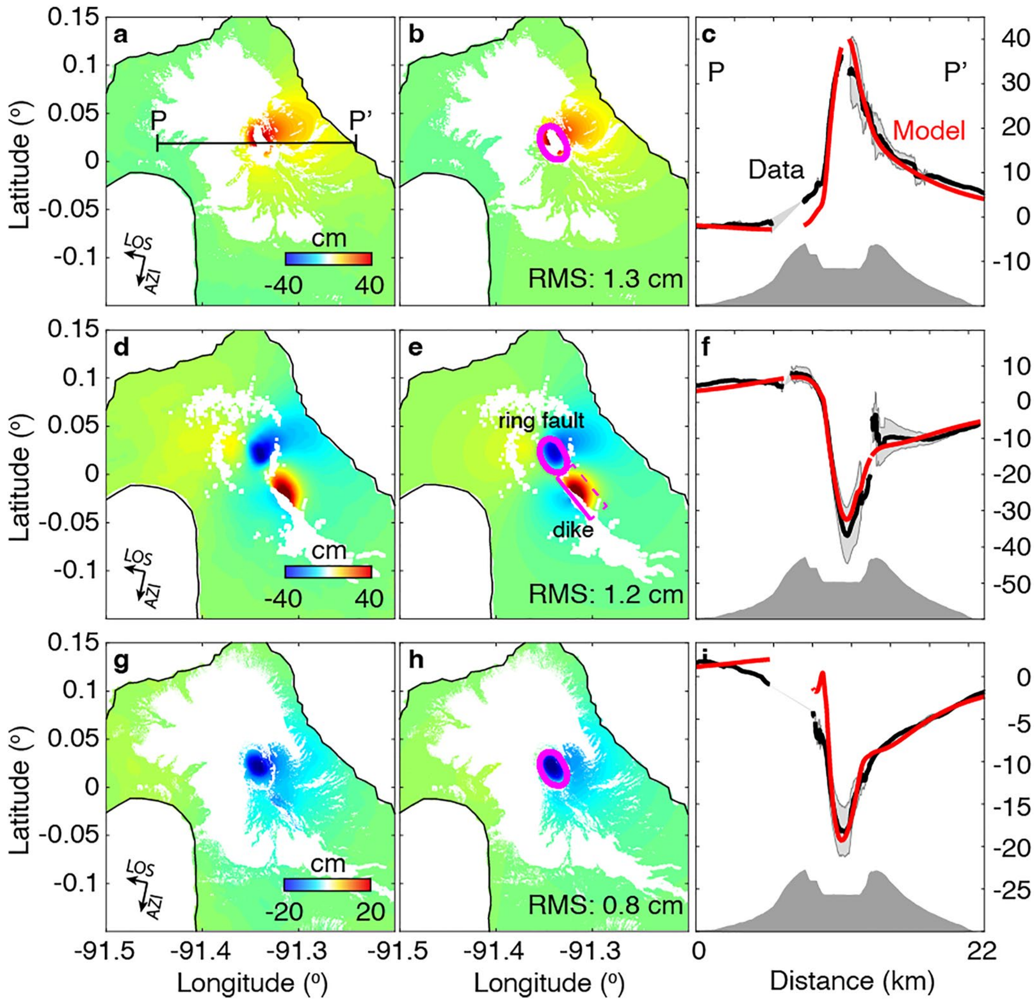

Figure 2. Unwrapped descending orbit InSAR data before, during and after the dike emplacement in comparison with model predictions. (a) Pre-eruption surface displacement in radar line-of-sight observed from Sentinel-1satellite (7 January 2017–5 January 2022) and (b), modeled displacement. (c), Observed (black, with gray shaded one-sigma error envelope) and modeled (red) displacements along profile P-P'. (d–f), Same as a-c, but for the 2022 co-eruption displacements obtained from the ALOS-2 satellite (2 January 2022–13 February 2022). (g–i), Same as a-c, but showing the post-dike emplacement deformation from Sentinel-1 satellite (29 January 2022–14 September 2022).

a distinct pattern of volcano-wide deformation with the maximum LOS displacement of ∼34 cm located near the center of the caldera (Figures 2a–2c and Figure S2 in Supporting Information S1). The similar deformation pattern in both ascending and descending orbits (Figure S2 in Supporting Information S1) suggests that the ground deformation is dominated by surface uplift. The descending-orbit InSAR time-series shows that the inner caldera started to uplift immediately after the 2015 eruption, with an average LOS uplift rate of about 6 cm/yr in both orbits (Figure S2 in Supporting Information S1).

3.2. The January 2022 Eruption and Post-eruptive Deformation

We used the ALOS-2 descending data collected on 2 January 2022 and 13 February 2022, Sentinel-1 descending data on 5 January 2022 and 29 January 2022 and ascending data on 4 January 2022 and 9 February 2022 to generate three co-eruptive interferograms. The observed ground deformation resembles that associated with previous eruptions from radial fissures at Fernandina volcano in 1995 and 2009 (Bagnardi et al., 2013; Chadwick et al., 2011; Jónsson et al., 1999). The descending ALOS-2 and Sentinel-1 interferograms are consistent and show a local, semi-circular zone of positive LOS displacement on the eastern side of the radial fissure, which is superimposed on a broad area of negative LOS displacement covering the summit caldera and a large part of the island (Figures 2d–2f and Figure S3 in Supporting Information S1). The ascending Sentinel-1 interferogram shows negative LOS

10.1029/2023GL103704

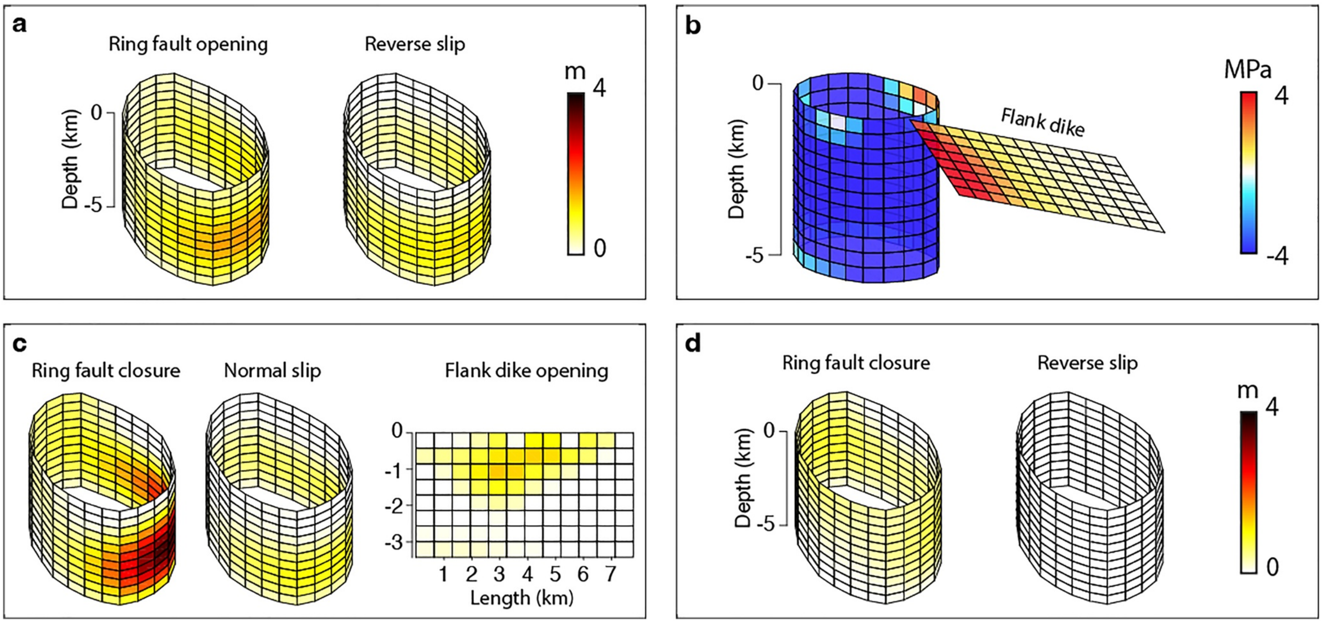

Figure 3. Inversion results and tensile stress changes of the caldera ring fault and flank dike. (a) Opening and reverse fault slip along the modeled ring dike before the 2022 eruption. (b) Tensile stress changes caused by caldera inflation before the 2022 eruption. The source fault is the modeled vertical ring fault, and the targeted receivers are the radial dike and the ring fault itself, respectively. Positive tensile stress changes (red) indicate unclamping of the dike plane, whereas the ring fault is under compression due to opening (blue). (c) Co-eruption closure and normal fault slip along the modeled ring dike and opening along the modeled flank dike during the 2022 eruption, respectively. d, Only ring-fault closure is found after the 2022 eruption.

displacements covering both the summit and the eruptive fissure. This suggests that the summit is dominated by subsidence, while the eruptive fissure has caused significant horizontal ground deformation on the flank.

Considering that the InSAR data are much less sensitive to north-south displacements, we also calculate the azimuth offsets using the ALOS-2 data (Figure S3 in Supporting Information S1). The interferograms and the azimuth-offset measurements reveal the complete 3D ground deformation covering the 2022 eruption. The 3D displacement map shows a broad, volcano-wide subsidence zone, with the maximum subsidence of about 56 cm centered on the caldera (Figure 1c). The deformation signals on the southeast flank are caused by the dike intrusion and eruptive fissure showing up to 34 cm of uplift and 70 cm of horizontal displacement.

The stack of post-eruptive descending Sentinel-1 interferograms between 29 January 2022 and 14 September 2022 shows a broad area of negative LOS displacement covering the edifice with a maximum LOS displacement of 5 cm, indicating that the volcano continued to subside after the 2022 eruption (Figures 2g–2i). Localized subsidence is also clearly seen over the parts of the flank dike that did not reach the surface close to the summit.

3.3. Geodetic Modeling Results

The observed pre-eruptive deformation can be explained by our ring fault model with both reverse faulting and opening (Figure 3a). The modeling results show that the caldera deformation is highly asymmetric, with the majority of fault slip occurring along the southern caldera rim, where the eventual eruptive activity occurred (Bernard et al., 2022). The model fits the deformation data well with an RMS value of 1.3 cm. The largest opening and reverse fault motions occurred at depths between 2.5 and 5 km with the maximum opening of 1.6 m at 3.5 km and reverse slip of 1.2 m at 4 km depth. A total volume change of about 3.8×10^7 m^3 (Table S3 in Supporting Information S1) is estimated to have been intruded as magma within the ring fault prior to the 2022 eruption and after July 2015, indicating that the average annual magma inflow rate was about 0.6×10^7 m^3/yr.

The co-eruptive deformation indicates a combination of two major deforming sources: the radial dike expanding with magma and ring faulting and volume loss along the inner caldera. This summit ring fault and radial dike model accurately reproduce the elliptical deformation pattern (Figures 2d–2f and Figure S3 in Supporting Information S1). The RMS misfit between the ALOS-2 data and the model is 1.2 cm. The radial dike was found to be dipping 58° to the northeast in the southeast flank with a maximum opening of 1 m at the surface. The strike of the dike was fixed at 141°, matching the eruptive fissures. The best fit model includes normal-faulting of the ring fault of up to 1 m at depths between 2 and 5 km (Figure 3c). In addition, the average closure of the caldera ring fault at 1–5 km in the best-fit model is about 0.4 m, which can explain the widespread subsiding pattern in the post-eruptive period. A total volume of about 3.8×10^7 m^3 is estimated from the inversion of pre-2022 inflation data to have been extruded before the 2022 eruption, whereas during the 2022 eruption about 5.5×10^7 m^3 is associated with the ring dike closure and about 0.7×10^7 m^3 the flank dike opening (Table S3 in Supporting Information S1). It should be noted that this calculation assumes that the difference between the ring dike closure and flank dike opening provides an estimate of extruded volume. The two-sill model and the combined ring-fault-sill model also show a good fit to the data, but the RMS misfit is higher. The best-fit two-sill model suggests that the deep sill is about 8 km long and 4 km wide, oriented NE-SW and deflates by 0.6 m, while the shallow sill is smaller in size (Table S4 in Supporting Information S1). The best-fit combined ring-fault-sill model suggests that the ring fault slip can produce similar deformation as that of the shallow sill. The ring fault closure model also fits well with the observed 2015 eruptive deformation (Figure S4 in Supporting Information S1) and the post 2022 eruptive deformation leading to a volume decrease of 6.1×10^7 m^3 and 2.3×10^7 m^3, respectively (Table S3 in Supporting Information S1).

To assess the stress interaction between the caldera inflation and the 2022 flank radial dike emplacement, we calculated the tensile stress changes on the 2022 radial dike plane resulting from the modeled ring fault sources within the Wolf magmatic system (Figure 3b). The stress change modeling shows that the pre-eruption opening and slip on the ring fault system unclamped (positive tensile stress change) the 2022 radial dike plane with the largest unclamping of over 4 MPa occurring at the end to the dike plane closest to the ring fault. This suggests that the stress changes caused by the preceding caldera ring fault activity promoted the emplacement of a radial dike on the SE volcano flank in 2022. This is similar to the idea that circumferential and radial dikes may alternate in time, proposed by Chadwick and Dieterich (1995). In comparison, the deep sill model causes only minor positive normal stress changes along the dike plane (Figure S5 in Supporting Information S1).

4. Discussions

Several recent studies of volcanoes in the western Galápagos Islands have suggested that the structure of the plumbing system involves hydraulically connected shallow crustal reservoirs located below the summit calderas at different depths or a combination of a ring fault system and a single deep magma reservoir (Bagnardi et al., 2013; Bell et al., 2021; Chadwick et al., 2011; Liu et al., 2019; Xu et al., 2016). In these models, the broad volcano-wide deformation during the co-eruptive period is mainly caused by volume decrease of the deep magma reservoir, whereas the ring fault motion or contraction of a shallow magma reservoir localizes subsidence within the caldera. However, the shape of the deep source would need to be elongated in one direction to fit the broad asymmetrical ground deformation at Wolf volcano (Figures S6 and S7 in Supporting Information S1). Although both the existing two-sill model (Xu et al., 2016) and the combined ring-fault-sill model (Liu et al., 2019) fit the volcano-wide deformation well, they left the ground deformation around the summit unexplained. Our proposed ring fault opening/closure model does not include a deep magma reservoir explicitly, but it fits all observed co-eruptive ground deformation with the lowest RMS misfits and outperforms the previous two-sill model and the combined ring-fault-sill model (Figures S6 and S7 in Supporting Information S1). Our model is consistent with the modeling results of Chadwick and Dieterich (1995) in that the ring fault activity makes the eventual radial dike more likely. This implies that the asymmetrical opening/closure of the model ring fault can produce volcano-wide deformation similar to that caused by a deep magma reservoir. These results highlight that the influence of a caldera ring fault that can open and close needs to be considered in addition to a reversal of ring fault slip when studying ground deformation at Wolf volcano.

Interestingly, recent eruptions have tended to be repeated within the same sector on individual Galápagos volcanoes (Figure 1a): Sierra Negra in the north, Fernandina in the south, Cerro Azul in the east and Wolf in the southeast, including both radial and circumferential eruptions. Asymmetrical kinematics of ring-fault motion has been observed during the 1968 Fernandina caldera collapse, the 2000 Miyakejima eruption, the 2014 Bárdarbunga caldera eruption (Glastonbury-Southern et al., 2022; Li et al., 2021) and the 2018 Kilauea caldera collapse (Anderson et al., 2019). During the 1968 trapdoor collapse of Fernandina caldera (Howard et al., 2018), the southeastern part of the caldera dropped more than 300 m, while only minor subsidence occurred on the opposite side. During the 2000 Miyakejima eruption, the asymmetrical collapse took place along an elliptical caldera ring fault on one side of the caldera floor. The onset of the 2018 eruption at Sierra Negra included intra-caldera reverse faulting and shallow magma migration in the north (Bell et al., 2021). The presence of intra-caldera

10.1029/2023GL103704

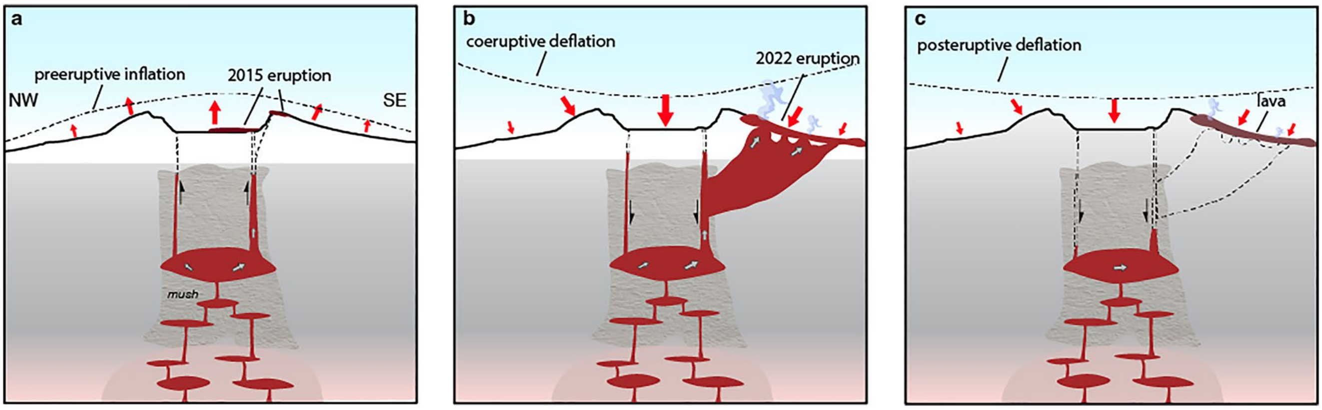

Figure 4. Schematic cartoon illustrating the preferred scenario of the magma plumbing system of Wolf volcano. (a) Pre-eruptive inflation and reverse ring-fault motion. (b) Radial dike emplacement, co-eruptive deflation, and normal faulting on the ring fault. (c) Post-eruptive deflation. The figure is not to scale for visualization.

benches formed during at least two historical collapses on the western side of Wolf volcano and fresh subaerial lavas seen in the southeast, suggest that the southeastern side of the volcano is now more active and the magma bodies may have shifted laterally through time (Geist et al., 2005). This implies that asymmetrical caldera collapse continues to be most likely on the southeastern side of Wolf volcano in the future. It is also interesting that Wolf exhibits a similar alternating cycle between radial and circumferential eruptions as on Fernandina and Cerro Azul volcanoes, with radial eruptions in 1982 and 2022, but a circumferential intrusion in 2015 (Bagnardi & Amelung, 2012; Xu et al., 2016). This shows how the stresses imposed by one eruption can influence the next; a caldera-inflation triggered dike intrusion and fissure eruption can lead to local rotations of the principal stress field that in turn influences future eruption patterns (Chadwick & Dieterich, 1995).

Magma migration from depth to intrude the crust or erupt at the surface can produce different types of volcanic earthquakes that are specific to caldera ring faults (Shuler et al., 2013). The estimated moment of the modeled shear-dislocation sources associated with the 2022 eruption corresponds to an earthquake of magnitude 5.9, assuming a shear modulus of 30 GPa. This is comparable to the largest reported event of Mw 5.4 during the onset of the 2018 eruption at Sierra Negra volcano (Vasconez et al., 2018). However, the largest reported earthquake during the time interval was a Mw 2.4 event, prior to the eruption (Bernard et al., 2022). Since earthquake records cannot account for the estimated moment release, ring fault activity likely involves dominantly aseismic shear and opening of a magma-filled fault zone.

Caldera collapse happens when a deep magma chamber drains rather abruptly. The presence of large calderas in the western Galápagos Islands indicates that these volcanoes have repeatedly undergone such collapses in their history. Our results suggest that magma intruded into the deep crustal reservoir beneath the caldera and exerted pressure on the piston beneath the caldera causing the upward motion along the ring fault and opening during the inflation period prior to the 2022 eruption (Figure 4). The repeated fault slip and opening of the caldera-bounding ring fault promoted the vertical and radial propagation of magma. The downward motion and closure of the caldera ring fault during the 2022 eruption likely occurred because the magma pressure in the system dropped and the magma reservoir roof collapsed as magma was fed to the surface. The caldera ring fault can thus involve both opening-mode fractures and dip-slip structures, which are important to consider in future modeling. Our study highlights that the asymmetry of ring fault activity influences the eruptive styles, locations, and patterns at Wolf volcano. Similar mechanisms of magma storage, edifice structures, and eruptive processes may occur at other caldera volcanos in the Galápagos Islands.

Conflict of Interest

The authors declare no conflicts of interest relevant to this study.

Data Availability Statement

ALOS-2 data (No. ER3A2N521) can be downloaded from https://gportal.jaxa.jp/gpr/. Sentinel-1 data can be downloaded from: https://search.asf.alaska.edu/#/. The processed unwrapped InSAR data used in this study can be found in Zenodo (https://doi.org/10.5281/zenodo.7747484).

Acknowledgments
We thank Bill Chadwick and Dennis Geist for their constructive comments and suggestions. We thank Sigurjón Jónsson for the early discussion about the eruption. This research was supported by Jilin Changbaishan Volcano National Observation and Research Station (No. NORSCBS20-04), National Key Research and Development Program (No. 2022YFB3903602), Frontier Cross Research Project of Central South University (No. 2023QYJC006), and National Natural Science Foundation of China (No. 42174023).

References

Amelung, F., Jónsson, S., Zebker, H., & Segall, P. (2000). Widespread uplift and 'trapdoor' faulting on Galápagos volcanoes observed with radar interferometry. *Nature*, *407*(6807), 993–996. https://doi.org/10.1038/35039604

Anderson, K. R., Johanson, I. A., Patrick, M. R., Gu, M., Segall, P., Poland, M. P., et al. (2019). Magma reservoir failure and the onset of caldera collapse at Kīlauea volcano in 2018. *Science*, *366*(6470), eaaz1822. https://doi.org/10.1126/science.aaz1822

Bagnardi, M., & Amelung, F. (2012). Space-geodetic evidence for multiple magma reservoirs and subvolcanic lateral intrusions at Fernandina volcano, Galápagos Islands. *Journal of Geophysical Research*, *117*(B10), B10406. https://doi.org/10.1029/2012JB009465

Bagnardi, M., Amelung, F., & Poland, M. P. (2013). A new model for the growth of basaltic shields based on deformation of Fernandina volcano, Galápagos Islands. *Earth and Planetary Science Letters*, *377*(378), 358–366. https://doi.org/10.1016/j.epsl.2013.07.016

Bechor, B. D. N., & Zebker, H. A. (2006). Measuring two-dimensional movements using a single InSAR pair. *Geophysical Research Letters*, *33*(16), L16311. https://doi.org/10.1029/2006GL026883

Bell, A. F., La Femina, P. C., Ruiz, M., Amelung, F., Bagnardi, M., Bean, C. J., et al. (2021). Caldera resurgence during the 2018 eruption of Sierra Negra volcano, Galápagos Islands. *Nature Communications*, *12*(1), 1397. https://doi.org/10.1038/s41467-021-21596-4

Bernard, B., Ramón, P., García, L., Hernandez, S., Vasconez, F. J., Viracucha, G., & Hidalgo, S. (2022). Volcanic event management in the Galápagos Islands, Ecuador. *Volcanica*, *5*(1), 209–225. https://doi.org/10.30909/vol.05.01.209225

Bernard, B., Stock, M. J., Coppola, D., Hidalgo, S., Bagnardi, M., Gibson, S., et al. (2019). Chronology and phenomenology of the 1982 and 2015 Wolf volcano eruptions, Galápagos archipelago. *Journal of Volcanology and Geothermal Research*, *374*, 26–38. https://doi.org/10.1016/j.jvolgeores.2019.02.013

Cervelli, P., Murray, M. H., Segall, P., Aoki, Y., & Kato, T. (2001). Estimating source parameters from deformation data, with an application to the March 1997 earthquake swarm off the Izu Peninsula, Japan. *Journal of Geophysical Research*, *106*(B6), 11217–11237. https://doi.org/10.1029/2000jb900399

Chadwick, W. W., & Dieterich, J. H. (1995). Mechanical modeling of circumferential and radial dike intrusion on Galápagos volcanoes. *Journal of Volcanology and Geothermal Research*, *66*(1–4), 37–52. https://doi.org/10.1016/0377-0273(94)00060-t

Chadwick, W. W., & Howard, K. A. (1991). The pattern of circumferential and radial eruptive fissures on the volcanoes of Fernandina and Isabela Islands, Galápagos. *Bulletin of Volcanology*, *53*(4), 259–275. https://doi.org/10.1007/BF00414523

Chadwick, W. W., Jónsson, S., Geist, D. J., Poland, M., Johnson, D. J., Batt, S., et al. (2011). The May 2005 eruption of Fernandina volcano, Galápagos: The first circumferential dike intrusion observed by GPS and InSAR. *Bulletin of Volcanology*, *73*(6), 679–697. https://doi.org/10.1007/s00445-010-0433-0

Fattahi, H., Agram, P., & Simons, M. (2017). A network-based enhanced spectral diversity approach for TOPS time-series analysis. *IEEE Transactions on Geoscience and Remote Sensing*, *55*(2), 777–786. https://doi.org/10.1109/TGRS.2016.2614925

Fattahi, H., & Amelung, F. (2013). DEM error correction in InSAR time series. *IEEE Transactions on Geoscience and Remote Sensing*, *51*(7), 4249–4259. https://doi.org/10.1109/TGRS.2012.2227761

Fialko, Y., Simons, M., & Agnew, D. (2001). The complete (3-D) surface displacement field in the epicentral area of the 1999 Mw7.1 Hector Mine earthquake, California, from space geodetic observations. *Geophysical Research Letters*, *28*(16), 3063–3066. https://doi.org/10.1029/2001gl013174

Galetto, F., Hooper, A., Bagnardi, M., & Acocella, V. (2020). The 2008 eruptive unrest at Cerro Azul volcano (Galápagos) revealed by InSAR data and a novel method for geodetic modelling. *Journal of Geophysical Research: Solid Earth*, *125*(2), e2019JB018521. https://doi.org/10.1029/2019JB018521

Geist, D., Bergantz, G., & Chadwick, W. (2014). Galápagos magma chambers. In K. Harpp, E. Mittelstaedt, N. d'Ozouville, & D. Graham (Eds.), *The Galápagos: A natural laboratory for the Earth sciences* (Vol. 1, pp. 55–69). American Geophysical Union.

Geist, D. J., Harpp, K. S., Naumann, T. R., Poland, M., Chadwick, W. W., Hall, M., & Rader, E. (2008). The 2005 eruption of Sierra Negra volcano, Galápagos, Ecuador. *Bulletin of Volcanology*, *70*(6), 655–673. https://doi.org/10.1007/s00445-007-0160-3

Geist, D. J., Naumann, T. R., Standish, J. J., Kurz, M. D., Harpp, K. S., White, W. M., & Fornari, D. J. (2005). Wolf volcano, galápagos archipelago: Melting and magmatic evolution at the margins of a mantle plume. *Journal of Petrology*, *46*(11), 2197–2224. https://doi.org/10.1093/petrology/egi052

Glastonbury-Southern, E., Winder, T., White, R. S., & Brandsdóttir, B. (2022). Ring fault slip reversal at Bárðarbunga volcano, Iceland: Seismicity during caldera collapse and re-inflation 2014–2018. *Geophysical Research Letters*, *49*(21), e2021GL097613. https://doi.org/10.1029/2021gl097613

Gudmundsson, M. T., Jónsdóttir, K., Hooper, A., Holohan, E. P., Halldórsson, S. A., Ófeigsson, B. G., et al. (2016). Gradual caldera collapse at Bárdarbunga volcano, Iceland, regulated by lateral magma outflow. *Science*, *353*(6296), aaf8988. https://doi.org/10.1126/science.aaf8988

Hersbach, H., Bell, B., Berrisford, P., Hirahara, S., Horányi, A., Muñoz-Sabater, J., et al. (2020). The ERA5 global reanalysis. *Quarterly Journal of the Royal Meteorological Society*, *146*(730), 1999–2049. https://doi.org/10.1002/qj.3803

Howard, K. A., Simkin, T., Geist, D. J., Merlen, G., & Nolf, B. (2018). Large hydromagmatic eruption related to Fernandina Volcano's 1968 caldera collapse-Deposits, landforms, and ecosystem recovery. *Field Volcanology: A Tribute to the Distinguished Career of Don Swanson*, 385–408.

Ito, G., & Bianco, T. (2014). Patterns in the Galápagos magmatism arising from the upper mantle dynamics of plume-ridge interaction. In K. Harpp, E. Mittelstaedt, N. d'Ozouville, & D. Graham (Eds.), *The Galápagos: A natural laboratory for the earth sciences* (Vol. 1, pp. 245–261). American Geophysical Union.

Jónsson, S. (2002). Fault slip distribution of the 1999 MW 7.1 Hector mine, California, earthquake, estimated from satellite radar and GPS measurements. *Bulletin of the Seismological Society of America*, *92*(4), 1377–1389. https://doi.org/10.1785/0120000922

Jónsson, S., Zebker, H., Cervelli, P., Segall, P., Garbeil, H., Mouginis-Mark, P., & Rowland, S. (1999). A shallow-dipping dike fed the 1995 flank eruption at Fernandina volcano, Galápagos, observed by satellite radar interferometry. *Geophysical Research Letters*, *26*(8), 1077–1080. https://doi.org/10.1029/1999gl900108

Li, S., Sigmundsson, F., Drouin, V., Parks, M. M., Ofeigsson, B. G., Jónsdóttir, K., et al. (2021). Ground deformation after a caldera collapse: Contributions of magma inflow and viscoelastic response to the 2015–2018 deformation field around Bárðarbunga, Iceland. *Journal of Geophysical Research: Solid Earth*, *126*(3), e2020JB020157. https://doi.org/10.1029/2020JB020157

Lin, J., & Stein, R. S. (2004). Stress triggering in thrust and subduction earthquakes and stress interaction between the southern San Andreas and nearby thrust and strike-slip faults. *Journal of Geophysical Research*, *109*(B2), B02303. https://doi.org/10.1029/2003JB002607

Liu, Y. K., Ruch, J., Vasyura-Bathke, H., & Jónsson, S. (2019). Influence of ring faulting in localizing surface deformation at subsiding calderas. *Earth and Planetary Science Letters*, *526*, 115784. https://doi.org/10.1016/j.epsl.2019.115784

Massimetti, F., Coppola, D., Laiolo, M., Valade, S., Cigolini, C., & Ripepe, M. (2020). Volcanic hot-spot detection using Sentinel-2: A comparison with MODIS–MIROVA thermal data series. *Remote Sensing*, *12*(5), 820. https://doi.org/10.3390/rs12050820

Okada, Y. (1985). Surface deformation due to shear and tensile faults in a half-space. *Bulletin of the Seismological Society of America*, *75*(4), 1135–1154. https://doi.org/10.1785/bssa0750041135

Poland, M. P., & Carbone, D. (2016). Insights into shallow magmatic processes at Kīlauea volcano, Hawaiʻi, from a multiyear continuous gravity time series. *Journal of Geophysical Research: Solid Earth*, *121*(7), 5477–5492. https://doi.org/10.1002/2016jb013057

Rosen, P. A., Gurrola, E., Sacco, G. F., & Zebker, H. (2012). The InSAR scientific computing environment. In *EUSAR 2012, 9th European conference on synthetic aperture radar* (pp. 730–733).

Rowland, S. K., Harris, A. J. L., Wooster, M. J., Amelung, F., Garbeil, H., Wilson, L., & Mouginis-Mark, P. J. (2003). Volumetric characteristics of lava flows from interferometric radar and multispectral satellite data: The 1995 Fernandina and 1998 Cerro Azul eruptions in the western Galápagos. *Bulletin of Volcanology*, *65*(5), 311–330. https://doi.org/10.1007/s00445-002-0262-x

Shuler, A., Ekström, G., & Nettles, M. (2013). Physical mechanisms for vertical-CLVD earthquakes at active volcanoes. *Journal of Geophysical Research: Solid Earth*, *118*(4), 1569–1586. https://doi.org/10.1002/jgrb.50131

Simkin, T., & Siebert, L. (1994). *Volcanoes of the world: A regional directory, gazeteer, and chronology of volcanism during the last 10,000 years* (2nd ed.). Geoscience Press.

Stock, M. J., Bagnardi, M., Neave, D. A., Maclennan, J., Bernard, B., Buisman, I., et al. (2018). Integrated petrological and geophysical constraints on magma system architecture in the western Galápagos archipelago: Insights from Wolf volcano. *Geochemistry, Geophysics, Geosystems*, *19*(12), 4722–4743. https://doi.org/10.1029/2018gc007936

Teasdale, R., Geist, D., Kurz, M., & Harpp, K. (2005). 1998 eruption at Volcán Cerro Azul, Galápagos Islands: I. Syn-eruptive Petrogenesis. *Bulletin of Volcanology*, *67*(2), 170–185. https://doi.org/10.1007/s00445-004-0371-9

Vasconez, F. J., Ramón, P., Hernandez, S., Hidalgo, S., Bernard, B., Ruiz, M., et al. (2018). The different characteristics of the recent eruptions of Fernandina and Sierra Negra volcanoes (Galápagos, Ecuador). *Volcanica*, *1*(2), 127–133. https://doi.org/10.30909/vol.01.02.127133

Williams, C. A., & Wadge, G. (2000). An accurate and efficient method for including the effects of topography in three-dimensional elastic models of ground deformation with applications to radar interferometry. *Journal of Geophysical Research*, *105*(B4), 8103–8120. https://doi.org/10.1029/1999jb900307

Xu, W., & Jónsson, S. (2014). The 2007–8 volcanic eruption on Jebel at Tair Island (Red Sea) observed by satellite radar and optical images. *Bulletin of Volcanology*, *76*(2), 795. https://doi.org/10.1007/s00445-014-0795-9

Xu, W., Jónsson, S., Ruch, J., & Aoki, Y. (2016). The 2015 Wolf volcano (Galápagos) eruption studied using Sentinel-1 and ALOS-2 data. *Geophysical Research Letters*, *43*(18), 9573–9580. https://doi.org/10.1002/2016GL069820

Zhang, Y., Fattahi, H., & Amelung, F. (2019). Small baseline InSAR time series analysis: Unwrapping error correction and noise reduction. *Computers & Geosciences*, *133*, 104331. https://doi.org/10.1016/j.cageo.2019.104331